Thoughts on the Phase-Screen Model

Chuck Rino

October 16,2026

Abstract

A phase screen is a mathematical abstraction. The compelling reason for using a phase-screen as a scintillation model is that under the parabolic (narrow-propagation-angle) approximation there is a complete theory that predicts the free-space evolution of the intensity spectral density function (SDF) and the mutual coherence function (MCF) which define S4 and ROTI as functions of parameters that characterize the phase-screen SDF and the Fresnel scale.

Using phase-screen simulations and the supporting theory for interperting scintillation diagnostics relies on phase-screen equivalence, which *assumes* that there is a reference plane from which free propagation of an initiating complex field generates a statistically equivalent field at a distance implied by the Fresnel scale. Back-propagation identifies the location of a *realizable* complex excitation field that reproduces a statistically equivalent realization of the measured field. However, multiple-phase-screen (MPS) simulations are constrained only by split-step integration, which can accommodate homogeneous stochastic structure to the diffraction limit. This paper reviews critical differences between MPS equivalence and theoretical phase-screen results.

1 Introduction

The theory of propagation in a irregular transparent medium starts with the vector wave equation for time-harmonic fields

$$\nabla^2\mathbf{E}(\mathbf{r}) + k^2\mathbf{E}(\mathbf{r}) = -X(\mathbf{r})\overline{\chi}\mathbf{E}(\mathbf{r}) + \boldsymbol{\nabla}\left(\boldsymbol{\nabla}\cdot\mathbf{E}\right), \tag{1}$$

where $X(\mathbf{r})\overline{\chi}$ is a 3×3 complex matrix that characterizes the interaction of the field with the propagation medium. Propagation is formally defined by introducing a rectangular coordinate system with one axis serving as a propagation reference. In a uniform magnetic field $\overline{\chi}$ is constant. If the divergence term is neglected an eigenvector decomposition of $X(\mathbf{r})\overline{\chi}$ can be used to generate three coupled scalar equations of the form

$$\nabla^2\psi\left(x,y\right) + k^2\psi\left(x,y\right) = -k^2X\left(x,y\right)\psi\left(x,y\right), \tag{2}$$

where $\psi(x,y)$ represents a component of the transformed vector wavefield. If the medium is homogeneous, solutions to (2) are superpositions of two orthogonal plane-wave characteristics modes. However, a complete treatment of vector propagation in an inhomogeneous medium *requires* retention of the divergence term. Fortunately, at frequencies above HF solving (2) with $\sqrt{X(x,y)}$ interpreted as a scalar refractive index characterizes the complex modulation of a circularly polarized transverse vector field component.

Even so, pursuing general solutions to (2) following scalar-field propagation methods requires computationally-demanding application-specific procedures. However, *any* solution to (2) will support a two-dimensional Fourier decomposition, which can be used to construct a solution to the homogeneous equation as a superposition of plane-wave components. Similarly, in the absence of diffraction ($\nabla^2\psi(x,y) \sim 0$), advancing the field a small distance forward imposes an incremental phase perturbation. This observation invites a split-step calculation comprised of a incremental phase perturbation followed by free propagation. The spatial wavenumber, $\boldsymbol{\kappa}$, is the transverse component of a wave propagating along the direction $\boldsymbol{k} = [\boldsymbol{\kappa}, \kappa_z]$. The propagation angle with respect to the z axis is $\theta = 2\pi\kappa/k$, where $k = 2\pi f/c$.

When the free propagation of a field initiatied by a phase screen generates significant structure at large propagation angles phase-screen theory breaks down. The ramifications have been investigated by Sun et al. [1]. However, we know from ray theory that solutions to (2) support field concentrations that act as local sources. Consequently, the presence of structure at large propagation angles is not automatically excluded, no does it preclude split-step integration. Fully three-dimensional MPS simulations are feasible. However, because of invariance along magnetic field lines, two-dimensional propagation is particularly well matched to analyzing complex time series generated by a propagation path swept through a disturbed regions. Hereafter, only two-dimensional propagation will be considered.

An incremental phase realization is generated such that

$$\Phi_\phi(\kappa_y) = C_p \begin{cases} {\kappa_y}^{-p_1}, & \kappa_y \leq \kappa_0 \\ ({\kappa_0}^{p_2-p_1}){\kappa_y}^{-p_2}, & \kappa_y > \kappa_0 \end{cases} . \tag{3}$$

The complex field at x_n, $\psi_n(y)$ is multiplied by the incremental phase screen contribution to update the field:

$$\psi_{n+\delta}(y) = \psi_n(y)\exp\{ik\phi(y)\} \tag{4}$$

Let

$$\widehat{\psi}_{n+\delta}(\kappa_y) = \int \psi_{n+\delta}(y)\exp\{-i\kappa_y y\}\frac{d\kappa_y}{2\pi} \tag{5}$$

$$\begin{aligned}\psi_{n+1}(y) = \int \widehat{\psi}_{n+\delta}(\kappa_y)\left[\exp\{i\left(\sqrt{1-(\kappa_y/k)^2}-1\right)(k\rho_F)^2\}\right] \\ \times \exp\{i\kappa_y y\}d\kappa_y/(2\pi)\,,\end{aligned} \tag{6}$$

where $k = 2\pi f_c/c$, and $\rho_F = \sqrt{\Delta x/k}$ is the Fresnel scale. Narrow-angle propagation implies that there is no κ_y contribution as $\kappa_y \to k$. In that case, the factor in square brackets reduces to $\exp\{\pm i\left(\kappa_y \rho_F\right)^2/2\}$. Insofar as MPS is concerned, narrow-angle scatter is demonstrated by equivalence of results obtained with frequency and propagation distance changes that preserve ρ_F.

2 MPS Simulation of Extreme Scintillation

The defining equations, (4), (5), and (6) are written as integrations of continuous functions. It is understood that for applications each integration is replaced by a Riemann sum over a finite range such that:

$$\begin{aligned} y(n\Delta y) &= n\Delta y \text{ for } 0 \le n \le N-1 & (7)\\ \kappa_y(m) &= m\Delta\kappa \text{ for } -N/2 \le m \le N/2-1 & (8)\\ \Delta\kappa &= 2\pi/\left(N\Delta y\right) & (9) \end{aligned}$$

with $dy \sim \Delta y$ and $d\kappa_y \sim \Delta\kappa$. A a minimum sampling interval $\Delta z > 200\lambda$ was found empirically. Simulations details are described in Section 3 of Rino et al. [2]. MPS propagation through a uniformly structured region followed by free-propagation to an observation plane was used to generate realizations subtending 50 km. With $v_{\text{eff}} = 152.6$ mps the realizations as time series are representative of processed GNSS segments.

Phase screen realizations were generated for representative EPB structure with $p1 = 2.0$ and $p2 = 3.25$ and PPB structure with $p1 = 3.0$ and $p2 = 1.5$. In Rino et al. [2] turbulent strength was adjusted to produce extreme scintillation in the free-space propagation range, which is perfectly recovered with back propagation. To explore potential MPS limits turbulent strength was increased to generate strong focusing and saturation within the disturbed region. The MPS extent was increased from 30 to 50 km followed by free propagation to 250 km.

Figure 1 summarizes an EPB development with strong scintillation realized in the free-propagation range. The upper frame displays the PSD evolution with measured $S4$ overlaid, red indicating MPS and blue indicating free-space. Spatial wave number has been converted to a direction angle $\theta = 2\pi\kappa_y/k$. In free space the PSD is invariant, whereby the initiating phase structure determines the range of propagation angles independent of evolving amplitude structure. The middle and lower frames show, respectively, intensity and phase at the 250 km observation range. Figure 2 shows the same simulation with C_P increased by 30 dB. Here strong focusing ($S4 > 1$) develops within the layer with the contributing range of propagation angles spanning $\pm 90^\circ$ with speckle-like ($S4 = 1$) saturation structure.

Phase-screen scintillation theory predicts constant $S4 \ge 1$ limits as the Fresnel scale increases indenfitinitey Carrano and Rino [3], whereas MPS limits predict a limiting exponential distribution. Intensity PDFs are formally de-

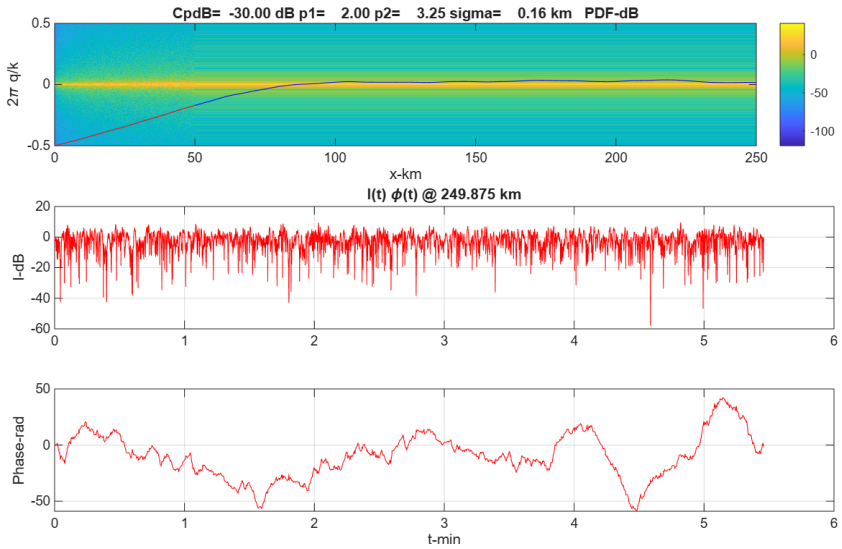


Figure 1: Top frame shows evolution of moderate EPB complex feld PSD versus radian propagation angle with $S4/2 + 0.5$ overlaid (0 to 1.5) red => MPS blue => free space. Middle and lower frames show intensity and phase versus time.

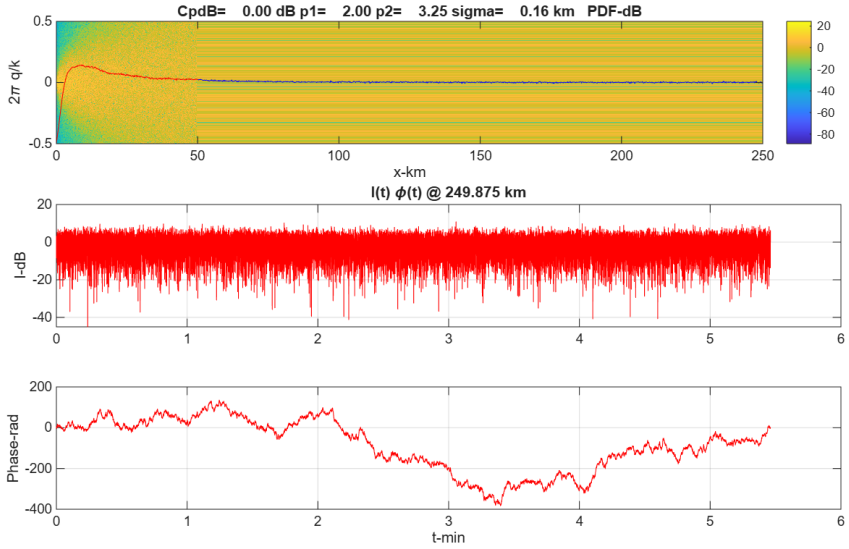


Figure 2: Evolution summary of strong EPB complex field. Same format as Figure 1

fined by fractional moments

$$M_m = < I^m > / < I >^m \ . \tag{10}$$

The critical moments are $m = 2$, 3, and 4. They define all the analytic intensity PDF models, often combined to define skew $K3 = (M_3 - 3M_2 + 2)/S4^{3/2}$ and kertosis $K4 = (M_4 - 4M_3 + 6M_2 - 3)/S4^2$, where $S4 = \sqrt{M_2 - 1}$. For an exponential distribution $M_m = m!$. Figure 3 summarizes the development of the fractional moments for the moderate (upper frame) and extreme (lower frame) simulations. Each moment is normalized to exponentional value to demonstrate convergence to exponentially distributed intensity scintillation with $S4 = 1$. By way of comparison, the phase-screen theoretical limits apply strictly to phase screens and break down if the correlation scale approaches the diffraction limit.

The peaks in the normalized fractional moments in the upper frame of Figure 3 are attributed to refractive changes induced by large-scale structure, which can vary significantly from realization to realization, achieving $K4$ values greater than 3. We also find that in the moderate to strong focusing regime the $\alpha - \mu$ distribution, which is defined by $K3$ and $K4$, provides a good fit to the intensity PDFs, in agreement with measured PDFs of measured scintillation. Figures 4, 5, and 6 shows the evolution of moderate and strong PPB structure. Surprisingly, the PPB does not generate strong focusing. This need further exploration, but it appears to provide a clear distinction between the evolution of EPB and PPB structure. We note also that saturation is achieved with much smaller C_p values. From phase-screen theory $S4$ is ordered by the universal strength parameter

$$U = C_P \begin{cases} \rho_F^{p_1 - 1} & \text{for } \mu_0 \leq 1 \\ \rho_F^{p_2 - 1} \mu_0^{p_1 - p_2} & \text{for } \mu_0 \leq 1 \end{cases} \ , \tag{11}$$

where $\mu_0 = \kappa_0 \rho_F$.

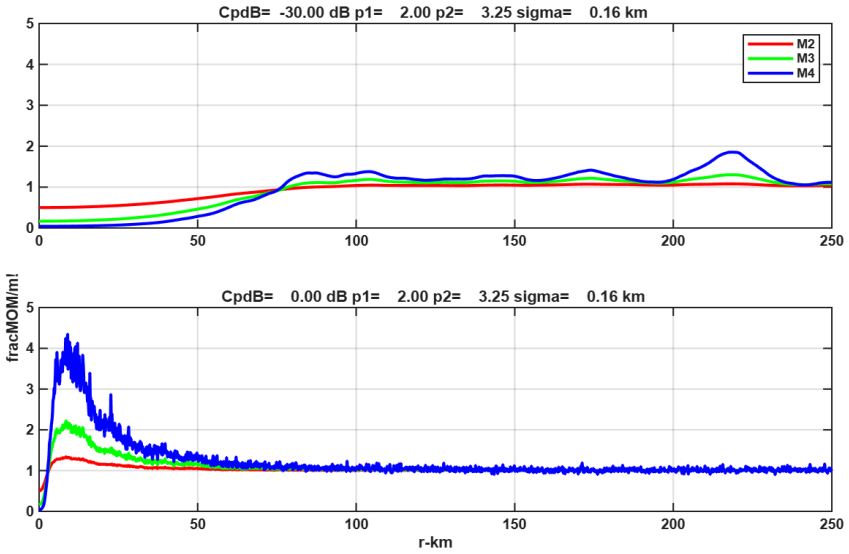


Figure 3: Moderate (upper frame) and strong (lower frame) evolution of fractional signal moments for EPB structure.

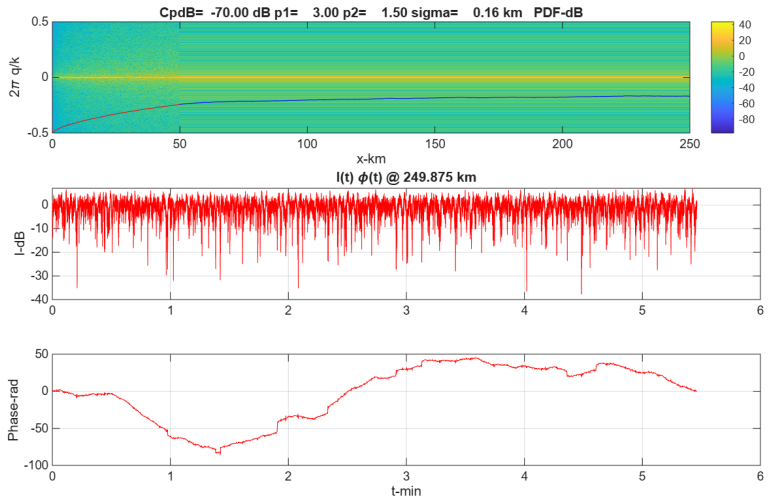


Figure 4: Top frame shows evolution of moderate PPB complex feld PSD versus radian propagation angle with $S4/2 + 0.5$ overlaid (0 to 1.5) red => MPS blue => free space. Middle and lower frames show intensity and phase versus time.

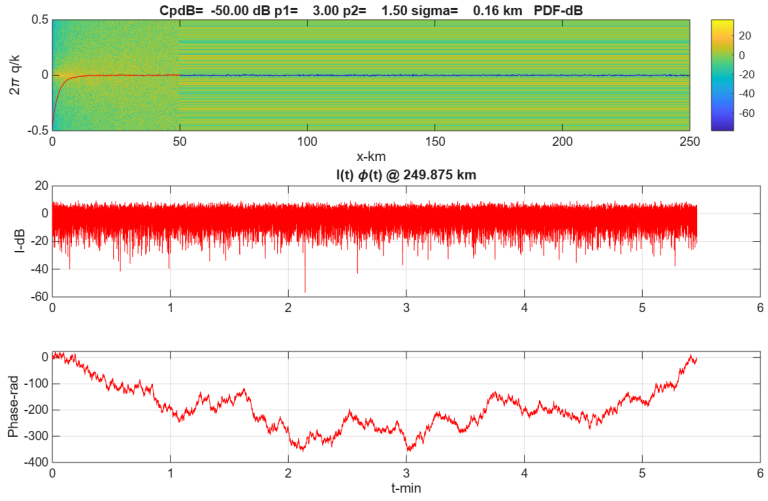


Figure 5: Evolution summary of strong PPB complex field. Same format as Figure 4

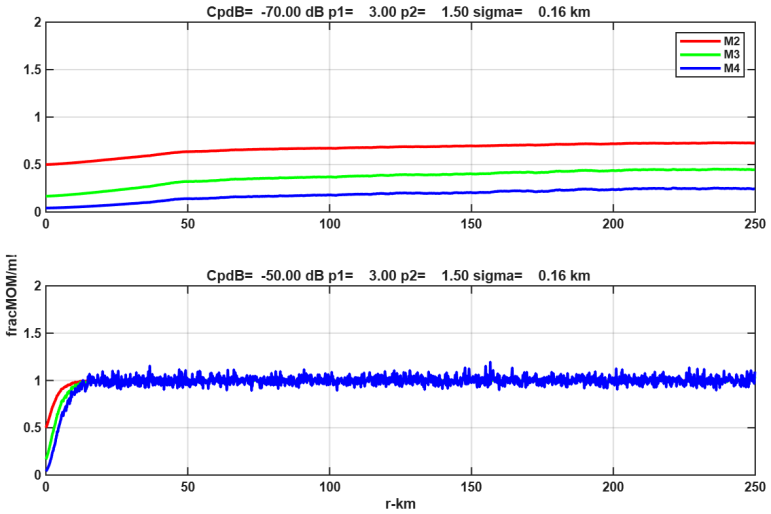


Figure 6: Moderate (upper frame) and strong (lower frame) evolution of fractional signal moments for PPB structure.

3 Discussion

In Rino et al. [2] MPS simulations were used to validate applying irregularity parameter estimation to reconstructed phase following back propagation. The purpose of this paper was to explore MPS simulations beyond the narrow propagation angle constraint. This is important because observations of extreme scintillation, particularly at UHF frequencies, can exceed the narrow-propagation-angle phase-screen theory limit. From previous analyses we know that for $S4 > 0.5$ unrecoverable cycle slips compromise recovery of absolute TEC measurements. However, it appears that surviving large-scale structure is sufficient to discriminate between EPB and PPB structure. Our investigation here shows that MPS simulations converge to speckle-like limit with an exponential PDF irrespective of the structure, with strong focusing favored by EPB structure.

3.1 Back Propagation

Back propagation (BP) is applied to the complex field at the observation range. For simulated data the complex field, $\psi(y;x)$, is constructed with unit intensity with spatial units. For real data, a detrending operation generates a complex time varying signal with unit intensity. An initial scan velocity estimate places the spatial Nyquist frequency at the smallest propagating wavenumber. A spatial Fourier transform of the complex field

$$\widehat{\psi}(\kappa_y) = \int \psi(y;xP)\exp\{-i\kappa_y y\}\frac{d\kappa_y}{2\pi} \tag{12}$$

initiated the BP operation. A minimization algorithm selects ρ_F that minimizes the variance of $\psi_{\rm BP}(y)$:

$$\psi_{\rm BP}(y) = \int \widehat{\psi}(\kappa_y) \left[\exp\{ i \left(\sqrt{1 - (\kappa_y/k)^2} - 1 \right) (k\rho_F)^2 \} \right] \times \exp\{ i\kappa_y y \} d\kappa_y / (2\pi) \,. \tag{13}$$

A starting value equal to the free-space propagation distance initiates the minimization operation. If no minimization is found the startng $\psi_{\rm BP}(y)$ is used. In real data low SNR or diffraction can cause a convergence failure indicated by a range larger than the initiating range.

Figures 7, 9, 11 and 13 compare the observation-plane intensity and phase (red) with the BP complex field intensity and phase (green). In all cases BP reduces the intensity variation in the observation plane. However, although although the phase unwraping algorithm eliminated phase changes larger than π radians, residual diffraction-induced phase errors remain. Even so, upon comparing measured phase SDFs with theoretical phase SDFs we see from Figures 8, 12, and 14 that EPB and PPB structure can be identified. The exception is Figure 10. Evidently, uncorrected diffraction effects can obscure EPB structure generating strong disturbances. A BP range larger than free-propagation distance, which can be estimated for a specified penetration point height is also a necessary condiction for successful BP.

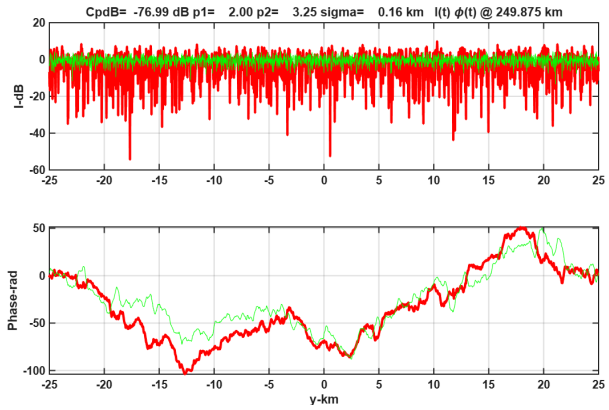


Figure 7: Upper frame reproduces EPB moderate intensity (red) with BP intensity overlaid (green)

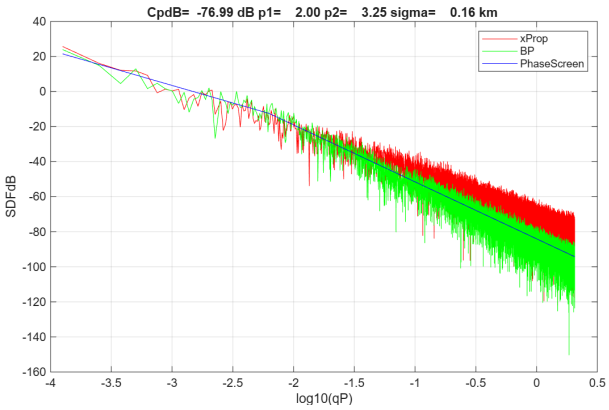


Figure 8: Moderate EPB phase SDF (red), reconstructed EPB phase SDF, (green), phase-screen SDF) blue.

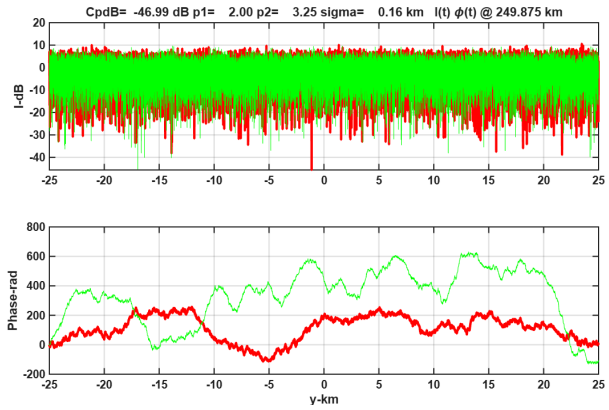


Figure 9: Upper frame reproduces EPB strong intensity (red) with BP intensity overlaid (green)

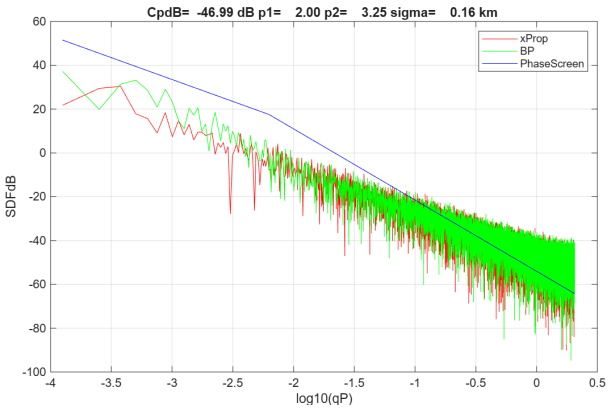


Figure 10: Strong EPB phase SDF (red), reconstructed EPB phase SDF, (green), phase-screen SDF) blue.

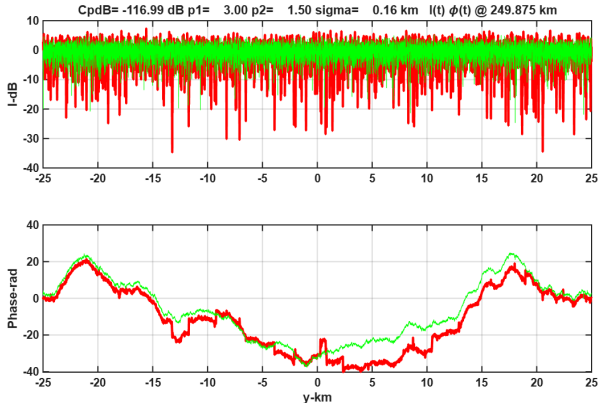


Figure 11: Upper frame reproduces PPB moderate intensity (red) with BP intensity overlaid (green)

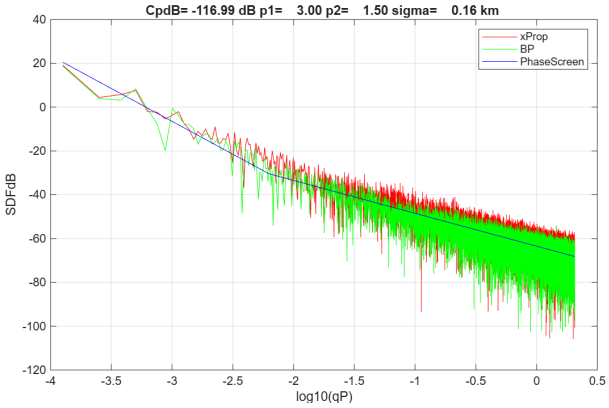


Figure 12: Moderate PPB phase SDF (red), reconstructed PPB phase SDF, (green), phase-screen SDF) blue.

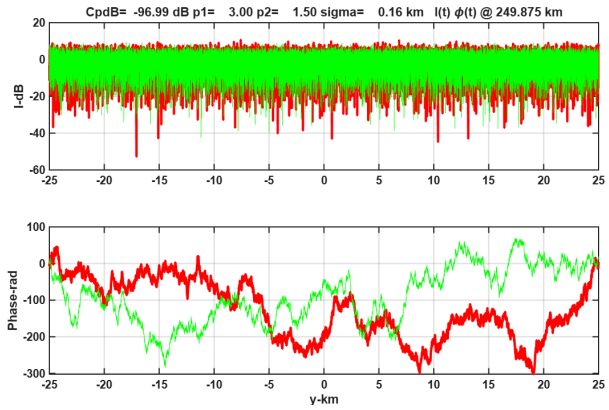


Figure 13: Upper frame reproduces PPB strong intensity (red) with BP intensity overlaid (green)

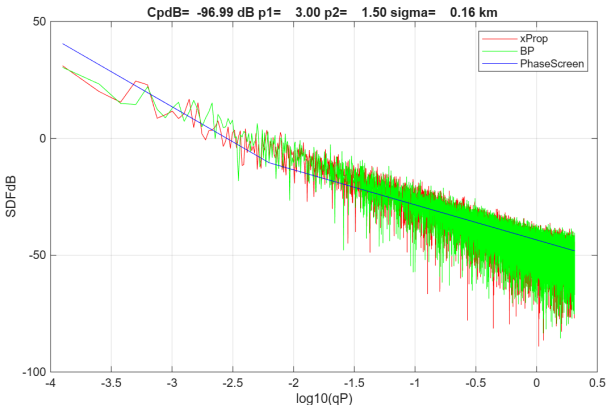


Figure 14: Strong PPB phase SDF (red), reconstructed PPB phase SDF, (green), phase-screen SDF) blue.

4 Summary

The analysis in this report was undertaken to reinforce the used of MPS simulations in Rino et al. [2] IPE to validate diagnostic procedures. In particular, we argued that the simulations are not constrained by the parabolic approximation. Extending the propagation disturbances to populate the full range of propagating structure suggest that a speckel-like limit is more representative of real data. Although the simulations indicate extreme scintillation can be generated under extreme conditions, BP is affected by diffraction and may not recover EPB structure. The results presented in this study show EPB structure can be obscured, but PPB structures are captured. In effec, indications of PPB structure are reflecting enhance large-scale structure. However, the unresolved two-component results may be associated with EPB structure. I effect, EPB structure is more sensitive to geometric effects and Diffraction effects.

References

[1] A. K. Sun, X. Pi, C. Rino, and J. Lee. Statistical uncertainty in the frequency dependence of the intensity scintillation index s4. *Radio Science*, 58, 2023. doi:org/10.1029/2023RS007659.

[2] Charles Rino, Charles Carrano, Dmytro Vasylyev, Theodore Beach, Brian Breitsch, Yu Morton, and Keith Groves. Extreme scintillation structure diagnostics. *Journal of Atmospheric and Solar Terrestial Physics*, 282, 2026. https://doi.org/10.1016/j.jastp.2026.106805.

[3] C. Carrano and C. Rino. A theory of scintillation for two-component power law irregularity spectra: Overview and numerical results. *Radio Science*, 51:789–813, 2016. doi:10.1002/2015RS005903.